# Generalization of Lambert's Reflectance Model

Michael Oren and Shree K. Nayar
Department of Computer Science, Columbia University
New York, NY 10027

## Abstract

Lambert's model for body reflection is widely used in computer graphics. It is used extensively by rendering techniques such as radiosity and ray tracing. For several real-world objects, however, Lambert's model can prove to be a very inaccurate approximation to the body reflectance. While the brightness of a Lambertian surface is independent of viewing direction, that of a rough surface increases as the viewing direction approaches the light source direction. In this paper, a comprehensive model is developed that predicts body reflectance from rough surfaces. The surface is modeled as a collection of Lambertian facets. It is shown that such a surface is inherently non-Lambertian due to the foreshortening of the surface facets. Further, the model accounts for complex geometric and radiometric phenomena such as masking, shadowing, and interreflections between facets. Several experiments have been conducted on samples of rough diffuse surfaces, such as, plaster, sand, clay, and cloth. All these surfaces demonstrate significant deviation from Lambertian behavior. The reflectance measurements obtained are in strong agreement with the reflectance predicted by the model.

**CR Descriptors:** I.3.7 [**Computer Graphics**]: Three-Dimensional Graphics and Realism; I.3.3 [**Computer Graphics**]: Picture/Image Generation; J.2 [**Physical Sciences and Engineering**]: Physics.

**Additional Key Words:** reflection models, Lambert's model, BRDF, rough surfaces, moon reflectance.

## 1 Introduction

An active area of research in computer graphics involves the creation of realistic images. Images are rendered using one of two well-known techniques, namely, ray tracing [36] or radiosity [7]. The quality of a rendered image depends to a great extent on the accuracy of the reflectance model used. In the past decade, computer graphics has witnessed the application of several physically-based reflectance models for image rendering (see [8], [17], [10], [14]). Reflection from a surface can be broadly classified into two categories: *surface* reflectance which takes place at the interface between two media with different refractive indices and *body* reflectance which is due to *subsurface scattering*. Most of the previous work on physically-based rendering has focused on accurate modeling of surface reflectance. They predict ideal specular reflection from smooth surfaces as well as wide directional lobes from rougher surfaces [14]. In contrast, the body component has most often been assumed to be Lambertian. A Lambertian surface appears equally bright from all directions. This model was advanced by Lambert [20] more than 200 years ago and remains one of the most widely used models in computer graphics.

For several real-world objects, however, the Lambertian model can prove to be a poor and inadequate approximation to body reflection. Figure 1(a) shows a real image of a clay vase obtained using a CCD camera. The vase is illuminated by a single distant light source in the same direction as the sensor. Figure 1(b) shows a rendered image of a vase with the same shape as the one shown in Figure 1(a). This image is rendered using Lambert's model, and the same illumination direction as in the case of the real vase. As


(a) (b)

Figure 1: (a) Real image of a cylindrical clay vase. (b) Image of the vase rendered using the Lambertian reflectance model. In both cases, illumination is from the viewing direction.

expected, Lambert's model predicts that the brightness of the cylindrical vase will decrease as we approach the occluding boundaries on both sides. However, the real vase is very flat in appearance with image brightness remaining almost constant over the entire surface. The vase is clearly *not* Lambertian[1]. This deviation from Lambertian behavior can be significant for a variety of real-world materials, such as, concrete, sand, and cloth. An accurate model that describes body reflection from such commonplace surfaces is imperative for realistic image rendering.

What makes the vase shown in Figure 1(a) non-Lambertian? We show that the primary cause for this deviation is the roughness of the surface. Figure 2 illustrates the relationship between magnification and reflectance (also see [17]). The reflecting surface may be viewed as a collection of planar facets. At high magnification, each picture element (rendered pixel) includes a single facet. At lower magnification, each pixel can include a large number of facets. Though the Lambertian assumption is often reasonable when look-

[1] Note that the real vase does not have any significant specular component, in which case, a vertical highlight would have appeared in the middle of the vase.

ing at a single planar facet, the reflectance is not Lambertian when a collection of facets is imaged onto a single pixel. This deviation is significant for very rough surfaces, and increases with the angle of incidence. In this paper, we develop a comprehensive model that predicts body reflectance from rough surfaces, and provide experimental results that support the model. Lambert's model is an instance, or limit, of the proposed model.

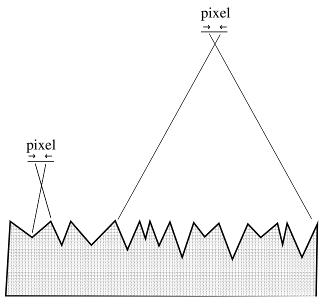


Figure 2: The roughness of a surface causes its reflectance properties to vary with image magnification.

The topic of rough surfaces has been extensively studied in the areas of applied physics, geophysics and engineering. The following is a brief summary of previous results on the subject. In 1924, Opik [25] designed an empirical model to describe the non-Lambertian behavior of the moon. In 1941, Minnaert [21] modified Opik's model to obtain the following reflectance function:

$$f_r = \frac{k+1}{2\pi}(\cos\theta_i \cos\theta_r)^{(k-1)} \qquad (0 \le k \le 1)$$

where, $\theta_i$ and $\theta_r$ are the polar angles of incidence and reflection, and $k$ is a measure of surface roughness. This function was designed to obey Helmholtz's reciprocity principle [2] but is not based on any theoretical foundation. It assumes that the radiance is symmetrical with respect to the surface normal. It will be shown in this paper that this assumption is incorrect. Hapke and van Horn [13] also obtained reflectance measurements from rough surfaces by varying the source direction for a fixed sensor direction. They found the peak of the radiance function to be shifted from the peak position expected for a Lambertian surface. They interpreted this as a minor discrepancy and concluded the Lambertian model to be a reasonable approximation. Our own measurements demonstrate that this non-Lambertian behavior is clearly noticeable and significant when viewer direction is varied rather than source direction.

The studies cited above were attempts to design reflectance models based on measured reflectance data. In contrast, Smith [30] and Buhl et al. [4] attempted to develop theoretical models for reflection from rough surfaces. These efforts were motivated primarily by reflectance characteristics of the moon. Visible and infrared emissions from the moon were recorded by a number of researchers (for examples, see [26] and [29]). These measurements indicate that the moon's surface reflects more light back in the direction of the source (the sun) than in the normal direction (like Lambertian surfaces) or in the forward direction (like specular surfaces). This phenomenon is referred to as *backscattering*. [2] Smith modeled the roughness of the moon as a random process and assumed each point on the surface to be Lambertian in reflectance. Smith's analysis, however, was confined to the plane of incidence and is not easily extensible to reflections outside this plane. Moreover, Smith's model does not account for interreflection effects. Buhl et al. [4] modeled the surface as a collection of spherical cavities. They analyzed interreflections using this surface model, but did not present a complete model that accounts for masking and shadowing effects for arbitrary angles of reflection and incidence. Subsequently, Hering and Smith [15] derived a detailed thermal emission model for surfaces modeled as a collection of V-cavities. However, all cavities are assumed to be identical and aligned in the same direction, namely, perpendicular to the source-viewer plane. Further, the model is limited to the plane of incidence.

More recently, body reflection has emerged as a topic of interest in the graphics community. Poulin and Fournier [27] derived a reflectance function for anisotropic surfaces modeled as a collection of parallel cylindrical sections. Addressing a different cause for non-Lambertian reflectance from the one discussed here, Hanrahan and Krueger [11] used linear transport theory to analyze subsurface scattering from a multi-layered surface. Other researchers in graphics have numerically pre-computed fairly complex reflectance functions and stored the results in the form of look-up tables or coefficients of spherical harmonic expansion (for examples, see [5] [17] [35]). This approach, though practical in many instances, does not replace the need for accurate analytical reflectance models.

The reflectance model developed here can be applied to isotropic as well as anisotropic rough surfaces, and can handle arbitrary source and viewer directions. Further, it takes into account complex geometrical effects such as *masking*, *shadowing*, and *interreflections* between points on the surface. We begin by modeling the surface as a collection of long symmetric V-cavities. Each V-cavity has two opposing facets and each facet is assumed to be much larger than the wavelength of incident light. This surface model was used by Torrance and Sparrow [31] to describe incoherent directional component of surface reflection from rough surfaces. Here, we assume the facets to be Lambertian [3]. First, we develop a reflectance model for anisotropic surfaces with one type (facet-slope) of V-cavities, with all cavities aligned in the same direction on the surface plane. Next, this result is used to develop a model for the more general case of isotropic surfaces that have normal facet distributions with zero mean and arbitrary standard deviation. The standard deviation parameterizes the *macroscopic* roughness of the surface. The fundamental result of our work is that the body reflectance from rough surfaces is not uniform but increases as the viewer moves toward the source direction. This deviation from Lambert's law is not predicted by any previous reflectance model.

We present several experimental results that demonstrate the accuracy of our model. The experiments were conducted on real samples such as sand, plaster and cloth. In all cases, reflectance predicted by the model was found to be in strong agreement with measurements. The derived model has been implemented as a shading function in RenderMan [33]. We conclude by comparing real and rendered images of a variety of objects. These results demonstrate two points that are fundamental to computer graphics: (a) Several real-world objects have body reflection components that are significantly non-Lambertian. (b) The model presented in this paper can be used to create realistic images of a variety of real-world objects.

## 2 Radiometric Definitions

In this section, we define radiometric concepts that are used in the remainder of this paper. These concepts are discussed in detail in [23]. Figure 3 shows a surface element $dA$ illuminated from the direction $\hat{s} = (\theta_i, \phi_i)$ and viewed by a sensor (image pixel) in the direction $\hat{v} = (\theta_r, \phi_r)$. We use $\theta$ to denote polar angles and $\phi$ to

[2] A different backscattering mechanism, called retroreflection or opposition effect, produces a sharp peak close to the source direction (see [13, 19, 32, 24, 28, 12]). This is not the mechanism discussed in this paper.

[3] This assumption does not limit the implications of the reflectance model presented here. The non-Lambertian behavior reported here is expected for a wide range of local body reflectance models (see [6], for example) since surface roughness is shown to play a dominant role.

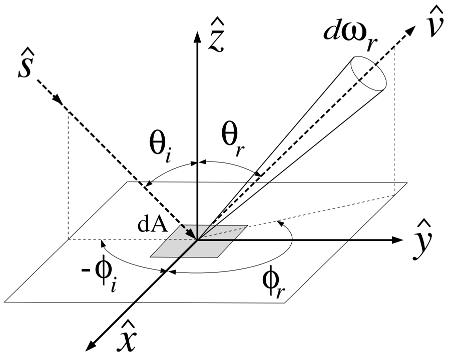


Figure 3: Geometry used to define radiometric terms.

denote azimuth angles. The sensor subtends an infinitesimal solid angle $d\omega_r$ from any point on the surface.

The light energy reflected by the surface patch is proportional to the light incident on the patch. *Irradiance* is defined as the light flux incident per unit area of the surface:

$$E(\theta_i, \phi_i) = \frac{d\Phi_i(\theta_i, \phi_i)}{dA} \tag{1}$$

This is the directional irradiance of the surface as it represents light energy incident from the direction $(\theta_i, \phi_i)$. The *total irradiance* of the surface is the flux incident from all directions and may be denoted simply as $E$. The brightness measured by the sensor is proportional to the *radiance* of the surface patch in the direction $(\theta_r, \phi_r)$. Surface radiance is defined as:

$$L_r(\theta_r, \phi_r; \theta_i, \phi_i) = \frac{d^2\Phi_r(\theta_r, \phi_r; \theta_i, \phi_i)}{dA \; \cos\theta_r \; d\omega_r} \tag{2}$$

It is the flux radiated by the surface per unit solid angle, per unit *foreshortened* area. It depends on the direction of illumination and the sensor direction. The relationship between irradiance and radiance of a surface is determined by its reflectance properties. The *bi-directional reflectance distribution function (BRDF)* is defined as the ratio of radiance to irradiance:

$$f_r(\theta_r, \phi_r; \theta_i, \phi_i) = \frac{dL_r(\theta_r, \phi_r; \theta_i, \phi_i)}{dE(\theta_i, \phi_i)} \tag{3}$$

All the above definitions are general, in that, they are valid for surfaces with any reflectance characteristics. For an *isotropic* surface, radiance and *BRDF* do not change if the surface is rotated about its normal vector. For such surfaces, the *BRDF* is simply:

$$f_r(\theta_r, \theta_i, \phi_r - \phi_i) = \frac{dL_r(\theta_r, \theta_i, \phi_r - \phi_i)}{dE(\theta_i)} \tag{4}$$

A special type of reflectance that is widely used for image rendering is *Lambertian* reflectance. A Lambertian surface is an ideal diffuser whose radiance is independent of the viewing direction of the sensor; it appears equally bright from all directions. Its *BRDF* is $f_r = \frac{\rho}{\pi}$ where $\rho$ is the *albedo* of the surface and represents the fraction of incident energy that is reflected by the surface.

## 3 Surface Roughness Model

There are several ways of modeling surface roughness. The general approach is to select a model that is capable of representing real surfaces and at the same time easy to use during the mathematical development of the reflectance model. All surface models found in applied physics and geophysics literature can be divided into two broad categories. In the first case, the surface is modeled as a random process (see [1, 34, 30]). Using this approach, it is difficult to derive a reflectance model for arbitrary source and viewer directions as well as to analyze interreflections. In the second category, surfaces are assumed to be composed of several elements with some primitive shape, for example, spherical cavities, V-cavities, holes, etc (see [4, 31]). As shown in this paper, the effects of shadowing, masking, and interreflections need to be modeled to obtain an accurate reflectance model. To achieve this, we use the roughness model proposed by Torrance and Sparrow [31] that assumes the surface to be composed of long symmetric V-cavities (see Figure 4) with their upper edges in the same plane. Each cavity consists of two planar facets. The width of each facet is assumed to be small compared to its length. The roughness of the surface is specified using a probability function for the distribution of facet slopes.

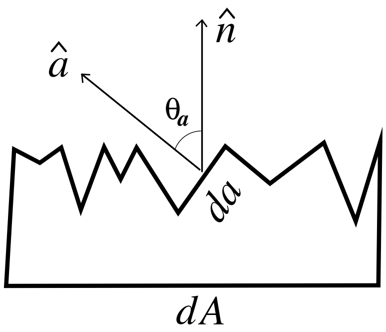


Figure 4: Surface modeled as a collection of V-cavities.

The V-cavity roughness model can be used to describe surfaces with both isotropic as well as anisotropic (directional) roughness. We assume each facet area $da$ is small compared to the area $dA$ of the surface patch that is imaged by a single sensor pixel. Hence, each pixel includes a very large number of facets. Further, the facet area is large compared to the wavelength $\lambda$ of incident light and therefore geometrical optics can be used to derive the reflectance model. The above assumptions can be summarized as:

$$\lambda^2 \ll da \ll dA \tag{5}$$

The facets could be relatively small as in the case of sand and plaster, or large as in the case of outdoor scenes of terrain.

**Slope-Area Probability Distribution**:

We denote the slope and orientation of each facet in the V-cavity model as $(\theta_a, \phi_a)$. Torrance and Sparrow have assumed all facets to have equal area $da$. They use the distribution $N(\theta_a, \phi_a)$ [4] to represent the number of facets per unit surface area that have the normal $\hat{a} = (\theta_a, \phi_a)$. Here, we use a probability distribution to represent the fraction of the surface area that is occupied by facets with a given normal. This is referred to as the *slope-area distribution* $P(\theta_a, \phi_a)$. The facet-number distribution and the slope-area distribution are related as follows:

$$P(\theta_a, \phi_a) == N(\theta_a, \phi_a) \, da \, \cos\theta_a \tag{6}$$

The slope-area distribution is easier to use than the facet-number distribution in the following model derivation. For isotropic surfaces, $N(\theta_a, \phi_a) = N(\theta_a)$ and $P(\theta_a, \phi_a) = P(\theta_a)$, since the distributions are rotationally symmetric with respect to the global surface normal $\hat{n}$ (Figure 4).

[4] In [31], $N(\theta_a, \phi_a)$ is denoted by $p(\alpha)$ where $\theta_a = \alpha$ and $\phi_a = 0$.

## 4 Reflectance Model

In this section, we derive a reflectance model for body reflectance from rough surfaces. The V-cavity model is used to describe surface geometry and each facet on the surface is assumed to be Lambertian in reflectance. The following three types of surfaces with different slope-area distributions are examined. (a) **Uni-directional Single-Slope Distribution:** This distribution results in a non-isotropic surface where all facets have the same slope and all cavities are aligned in the same direction. (b) **Isotropic Single-Slope Distribution:** Here, all facets have the same slope but they are uniformly distributed in orientation on the surface plane. (c) **Gaussian Distribution:** This is the most general case examined where the slope-area distribution is assumed to be normal with zero mean. The roughness of the surface is determined by the standard deviation of the normal distribution. The reflectance model obtained for each of the above surface types is used to derive the succeeding one.

**Effect of Roughness on Body Reflectance:**

Before we proceed to derive reflectance models for the above-mentioned surface types, a brief illustration of the effect of roughness on body reflection would be useful. Consider, for the purpose of discussion, the single V-cavity shown in Figure 5. Both facets of the cavity are fully illuminated by a distant source on the right side. If the facets are Lambertian with equal albedo, the left facet appears brighter than the right one as it receives more incident light. If the V-cavity is viewed from the left side by a distant observer, a larger fraction of the foreshortened cavity area is dark and a smaller fraction is bright. As the observer moves to the right, towards the source direction, the fraction of brighter area increases while that of the darker area decreases. Consequently, the total brightness, or radiance, of the cavity increases as the observer approaches the source direction. Note that this results from the brightness disparity between the two facets which increases with the angle of incidence. This effect is in contrast to Lambertian surfaces whose brightness does not vary with the viewing direction. The above illustration demonstrates that rough diffuse surfaces are inherently non-Lambertian in reflectance. Their radiance increases as the viewer approaches the source direction. Now we present a formal treatment of the above effects.

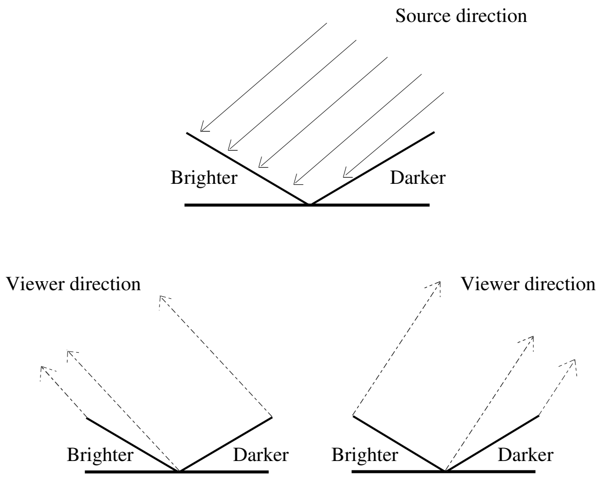


Figure 5: The radiance of the V-cavity increases as the viewer moves towards the illumination direction.

**The Projected Radiance:**

Consider surface area $dA$ that is imaged by a single sensor element in the direction $\hat{v} = (\theta_r, \phi_r)$ and illuminated by a distant point light source in the direction $\hat{s} = (\theta_i, \phi_i)$. The area $dA$ is composed of a very large number of symmetric V-cavities. Each V-cavity is composed of two facets with the same slope but facing in opposite directions. Our approach is to compute the radiance contribution of each facet on the surface. Then, the total radiance of the surface patch can be determined as an aggregate of the contributions of all facets. Consider the flux reflected by a facet with area $da$ and normal $\hat{a} = (\theta_a, \phi_a)$. The projected area on the surface occupied by the facet is $da \cos\theta_a$ (see Figure 4). Hence, while computing the contribution of the facet to the radiance of the surface patch, we need to use the projected area $da \cos\theta_a$ and not the actual facet area $da$. The radiance contribution thus determined is what we call the *projected radiance* of the facet:

$$L_{rp}(\theta_a, \phi_a) = \frac{d^2\Phi_r(\theta_a, \phi_a)}{(da \cos\theta_a) \cos\theta_r \, d\omega_r} \tag{7}$$

For ease of description, we have dropped the source and viewing directions from the notations for projected radiance and flux.

**Total Radiance:**

Now consider the slope-area distribution of facets given by $P(\theta_a, \phi_a)$. The total radiance of the surface can be obtained as the average of $L_{rp}(\theta_a, \phi_a)$ of all facets on the surface:

$$L_r(\theta_r, \phi_r; \theta_i, \phi_i) = \tag{8}$$
$$\int_{\theta_a=0}^{\frac{\pi}{2}} \int_{\phi_a=0}^{2\pi} P(\theta_a, \phi_a) \, L_{rp}(\theta_a, \phi_a) \, \sin\theta_a \, d\phi_a \, d\theta_a$$

Thus, we have decomposed the problem of computing the radiance of any rough surface to one of computing the projected radiance for each facet on the surface. The total radiance of the surface is then obtained by integrating the product of the projected radiance and the slope-area distribution function over all facet normals.

### 4.1 Model for Uni-directional Single-Slope Distribution

The first surface type we consider has all facets with the same slope $\theta_a$. Further, all V-cavities are aligned in the same direction; azimuth angles of all facets are either $\phi_a$ or $\phi_a + \pi$. The results obtained for this anisotropic surface will be used later in the analysis of isotropic surfaces.

**Radiance from a Lambertian Facet:**

Consider a Lambertian facet that is fully illuminated (no shadowing) and is completely visible (no masking) from the sensor direction. The radiance of the facet is proportional to its irradiance and is equal to $\frac{\rho}{\pi} E(\theta_a, \phi_a)$. The irradiance of the facet is $E(\theta_a, \phi_a) = E_0 < \hat{s}, \hat{a} >$, where, $E_0$ is the irradiance when the facet is illuminated head-on (i.e. $\hat{s} = \hat{a}$), and $<\,,\,>$ denotes the dot product between two vectors. Using the definition of radiance, the flux reflected by the facet in the sensor direction is obtained as:

$$d^2\Phi_r \;=\; \frac{\rho}{\pi} E_0 < \hat{s}, \hat{a} > < \hat{v}, \hat{a} > da \, d\omega_r \tag{9}$$

Substituting the above reflected flux in (7), we get:

$$L_{rp}(\theta_a, \phi_a) \;=\; \frac{\rho}{\pi} E_0 \frac{< \hat{s}, \hat{a} >< \hat{v}, \hat{a} >}{< \hat{a}, \hat{n} >< \hat{v}, \hat{n} >} \tag{10}$$

This expression clearly indicates that the projected radiance of a tilted Lambertian facet is not equal in all viewing directions. Consequently, a rough surface comprised of tilted Lambertian facets is non-Lambertian; its radiance varies with the viewing direction. *This phenomenon is observed even in the absence of masking, shadowing, and interreflection effects.*

### 4.1.1 Geometric Attenuation Factor

If the surface is illuminated and viewed from the normal direction ($\hat{s} = \hat{v} = \hat{n}$), all facets are fully illuminated and visible. For larger angles of incidence and reflection, however, facets are shadowed and masked by adjacent facets (see Figure 6). In the case of *shadowing*, a facet is only partially illuminated as the adjacent facet on the V-cavity casts a shadow on it. In the case of *masking*, the facet is only partially visible to the sensor as its adjacent facet occludes it. Both these geometrical phenomena affect the projected radiance of the facet and hence must be taken into account. The result is a *geometrical attenuation factor* ($\mathcal{GAF}$) that lies between zero and unity (also see [31] [3]). It is the reduction in the projected radiance of a facet due to masking and shadowing effects; it equals the ratio of the facet area that is both visible and illuminated, to the total facet area. The details of the derivation of the $\mathcal{GAF}$are given in appendix A The final result can be compactly represented as:

$$\mathcal{GAF} = Min\left[1, Max\left[0, \frac{2<\hat{s},\hat{n}><\hat{a},\hat{n}>}{<\hat{s},\hat{a}>}, \frac{2<\hat{v},\hat{n}><\hat{a},\hat{n}>}{<\hat{v},\hat{a}>}\right]\right] \tag{11}$$

The above $\mathcal{GAF}$ is valid for any facet normal, $\hat{a}$, not necessarily the bisector of the angle between the source and the sensor direction.

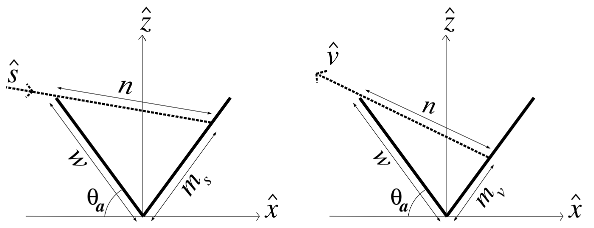

(a) (b)

Figure 6: (a) Shadowing and (b) masking in a V-cavity.

**Projected Radiance and $\mathcal{GAF}$:**

The projected radiance of a Lambertian facet is obtained by simply multiplying the geometric attenuation factor with the projected radiance (10) derived under the assumption of no masking and shadowing. Table 1 details the $\mathcal{GAF}$ and the corresponding projected radiance for all cases of shadowing and masking. Note that the projected radiance is denoted as $L^1_{rp}$; the superscript is used to indicate that the radiance is due to direct illumination by the source. In the next section, we will use $L^2_{rp}$ to denote radiance due to interreflections.

### 4.1.2 Interreflection Factor

In our reflectance model, we also account for interreflections; light rays bouncing between adjacent facets. These effects are significant for rough surfaces with relatively high albedo values. When the surface is illuminated from large angles ($\theta_i$) and viewed from the opposite side at large angles ($\theta_r$), none of the facets that are visible to the sensor are illuminated by the source. If interreflections are not considered, the radiance of the surface would be zero in this case. However, the visible facets receive light from their adjacent facets that face the source and hence are illuminated. These interreflections result in non-zero surface radiance. Our analysis and experimental results suggest that the contribution due to interreflections can be significant and cannot in general be ignored.

We have the task of modeling interreflections in the presence of masking and shadowing effects. In the case of Lambertian surfaces, the energy in an incident light ray diminishes rapidly with each interreflection bounce. Therefore, we model only two-bounce interreflections and ignore subsequent bounces. Simulations of the interreflection process were used to verify that this approximation is good.

In the following discussion, we refer to surface radiance due to direct illumination by the source as $L^1_r$ and radiance due to interreflections as $L^2_r$. We will use the same superscripts for projected radiance. The two-bounce interreflection component for a Lambertian facet can be expressed as [29] [18] [9] [22]:

$$L^2_r(\vec{\mathbf{x}}) = \frac{\rho}{\pi}\int\int K(\vec{\mathbf{x}},\vec{\mathbf{y}})L^1_r(\vec{\mathbf{y}})d\vec{\mathbf{y}} \tag{12}$$

where $\vec{\mathbf{x}}$ is a point on the facet whose interreflection component is determined as an integral of the radiance of all points $\vec{\mathbf{y}}$ on the adjacent facet. $K(\vec{\mathbf{x}},\vec{\mathbf{y}})$ is the *kernel* and represents the geometrical relationship between $\vec{\mathbf{x}}$ and $\vec{\mathbf{y}}$. Since the V-cavity is long compared to its width, it can be viewed as a one-dimensional shape with translational symmetry. For such shapes, the interreflection component can be determined as an integral over the one-dimensional cross-section of the shape. The above interreflection equation is therefore reduced to:

$$L^2_r(x) = \frac{\rho}{\pi}\int K'(x,y)L^1_r(y)dy \tag{13}$$

where $x$ and $y$ are the shortest distances of points $\vec{\mathbf{x}}$ and $\vec{\mathbf{y}}$ from the intersection of the two facets (see Figure 7). $K'$ is the kernel for the translational symmetry case and is derived in [16] and [9] to be:

$$K'(x,y) = \frac{\pi\sin^2(2\theta_a)}{2}\frac{xy}{(x^2+2xy\cos(2\theta_a)+y^2)^{3/2}} \tag{14}$$

We know that the normal of the considered facet is $\hat{a} = (\theta_a, \phi_a)$

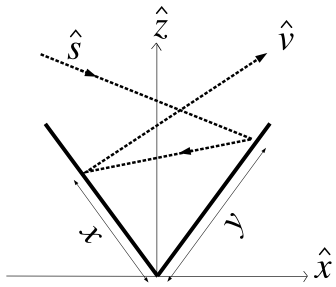

Figure 7: Interreflections in a V-cavity.

and the normal of the adjacent facet is $\hat{a}' = (\theta_a, \phi_a + \pi)$. The limits of the integral in the interreflection equation are determined by the masking and shadowing of these facets. As before, let $m_v$ be the width of the facet which is visible to the viewer. Let $m^s$ be the width of the *adjacent* facet that is illuminated. As in Section 4.1.1, expressions can be obtained for the visible and illuminated sections:

$$\frac{m_v}{w} = Max\left[0, Min\left[1, -\frac{<\hat{a}',\hat{v}>}{<\hat{a},\hat{v}>}\right]\right] \tag{15}$$

$$\frac{m^s}{w} = Max\left[0, Min\left[1, -\frac{<\hat{a},\hat{s}>}{<\hat{a}',\hat{s}>}\right]\right] \tag{16}$$

From the definition of projected radiance (7) and expression (13) we have:

$$L^2_{rp} = \frac{l<\hat{a},\hat{v}>}{da<\hat{a},\hat{n}><\hat{v},\hat{n}>}\int_{x=m_v}^{w}L^2_r(x)\,dx = \tag{17}$$

$$(\frac{\rho}{\pi})^2E_0\frac{l<\hat{a}',\hat{s}><\hat{a},\hat{v}>}{da<\hat{a},\hat{n}><\hat{v},\hat{n}>}\int_{x=m_v}^{w}\int_{y=m^s}^{w}K'(x,y)dy\,dx$$

| | $\mathcal{GAF}$ | $L^1_{rp}(\theta_a,\phi_a)$ |
|---|---|---|
| No Masking or Shadowing | 1 | $\frac{\rho}{\pi}E_0\frac{<\hat{s},\hat{a}><\hat{v},\hat{a}>}{<\hat{a},\hat{n}><\hat{v},\hat{n}>} = \frac{\rho}{\pi}E_0\cos\theta_i\cos\theta_a\Big(1+\tan\theta_i\tan\theta_a\cos(\phi_i-\phi_a)\Big)\Big(1+\tan\theta_r\tan\theta_a\cos(\phi_r-\phi_a)\Big)$ |
| Masking | $\frac{2<\hat{v},\hat{n}><\hat{a},\hat{n}>}{<\hat{v},\hat{a}>}$ | $\frac{\rho}{\pi}E_0\,2<\hat{s},\hat{a}> = \frac{\rho}{\pi}E_0\cos\theta_i\cos\theta_a\;2\Big(1+\tan\theta_i\tan\theta_a\cos(\phi_i-\phi_a)\Big)$ |
| Shadowing | $\frac{2<\hat{s},\hat{n}><\hat{a},\hat{n}>}{<\hat{s},\hat{a}>}$ | $\frac{\rho}{\pi}E_0\frac{2<\hat{s},\hat{n}><\hat{v},\hat{a}>}{<\hat{v},\hat{n}>} = \frac{\rho}{\pi}E_0\cos\theta_i\cos\theta_a\;2\Big(1+\tan\theta_r\tan\theta_a\cos(\phi_r-\phi_a)\Big)$ |

Table 1: Projected radiance of a facet for different masking/shadowing conditions.

Using the following change of variables: $t=\frac{x}{w}$ ; $r=\frac{y}{w}$, the radiance due to two-bounce interreflections given by (17) can be written as:

$$L^2_{rp} = (\frac{\rho}{\pi})^2 E_0 \frac{<\hat{a}',\hat{s}><\hat{a},\hat{v}>}{<\hat{a},\hat{n}><\hat{v},\hat{n}>}\int_{t=\frac{m_v}{w}}^{1}\int_{r=\frac{m^s}{w}}^{1} K'(t,r)dr\,dt \tag{18}$$

Using (14), the above integral is evaluated as:

$$\int_{t=\frac{m_v}{w}}^{1}\int_{r=\frac{m^s}{w}}^{1} K'(r,t)dr\,dt = \frac{\pi}{2}\left[d(1,\frac{m_v}{w})+d(1,\frac{m^s}{w})-d(\frac{m^s}{w},\frac{m_v}{w})-d(1,1)\right] \tag{19}$$

where:

$$d(x,y)=\sqrt{x^2+2xy\cos(2\theta_a)+y^2} \tag{20}$$

We refer to the right hand side of equation (19) as the *interreflection factor* ($\mathcal{IF}$). The total projected radiance of the facet is the sum of the projected radiance due to source illumination (given in Table 1) and the above interreflection component:

$$L_{rp}(\theta_a,\phi_a) \;=\; L^1_{rp}(\theta_a,\phi_a) \;+\; L^2_{rp}(\theta_a,\phi_a) \tag{21}$$

The uni-directional single-slope surface we have considered in this section has only two types of facets with normals $(\theta_a,\phi_a)$ and $(\theta_a,\phi_a+\pi)$. Hence, the radiance of the surface for any given source direction and sensor direction is simply the average of the projected radiances of the two facet types:

$$L_r(\theta_r,\phi_r;\theta_i,\phi_i;\theta_a,\phi_a)=\frac{L_{rp}(\theta_a,\phi_a)+L_{rp}(\theta_a,\phi_a+\pi)}{2} \tag{22}$$

## 4.2 Model for Isotropic Single-Slope Distribution

We now consider a surface with V-cavities that have facets with the same slope $(\theta_a)$, but uniformly distributed in orientation $(\phi_a)$ in the plane of the surface. The result is a surface with isotropic roughness. The reflectance model derived for this surface is based on the results obtained in the previous section for the single-slope surface. The results obtained in this section are important as they can be used to derive a reflectance model for any isotropic surface.

From the previous section, we know the radiance $L^1_{rp}(\theta_a,\phi_a)$ of a facet with normal $\hat{a}=(\theta_a,\phi_a)$. Therefore, the radiance of the single-slope isotropic surface due to direct source illumination is determined as an integral of the projected radiance over $\phi_a$:

$$L^1_{rp}(\theta_a) \;=\; \frac{1}{2\pi}\int_{\phi_a=0}^{2\pi} L^1_{rp}(\theta_a,\phi_a)d\phi_a \tag{23}$$

Given source direction $(\theta_i,\phi_i)$ and sensor direction $(\theta_r,\phi_r)$, we first need to find the ranges of facet orientation $\phi_a$ for which the facets are masked, shadowed, masked and shadowed, and neither masked nor shadowed[5]. The radiance for each range is given in Table 1. The problem then is to decompose the above integral into different parts, each corresponding to a different masking/shadowing range. We refer the interested reader to Appendix B.1 for details on the evaluation of integral (23). The final expression for surface radiance is found to be:

$$L^1_{rp}(\theta_a)=\frac{\rho}{\pi}E_0\cos\theta_i\cos\theta_a\Bigg[1+\cos(\phi_r-\phi_i)\Big(A_1(\alpha;\theta_a)\tan\beta+A_2(\beta,\phi_r-\phi_i;\theta_a)\Big)+(1-|\cos(\phi_r-\phi_i)|)A_3(\theta_r,\theta_i;\theta_a)\Bigg] \tag{24}$$

where, $\alpha=Max[\theta_i,\theta_r]$ and $\beta=Min[\theta_i,\theta_r]$. The expressions for the coefficients $A_1$, $A_2$, and $A_3$ are given in Appendix B.1. Note that the above projected radiance is the same as the total radiance of the surface ($L^1_r(\theta_r,\theta_i,\phi_r-\phi_i;\theta_a)=L^1_{rp}(\theta_a)$) since all facets on the surface have identical slope, $\theta_a$. The derivation in Appendix B.1 does not consider multiple reflections, as the interreflection component (19) is difficult to intergrate over all cavity orientations $\phi_a$. In Appendix B.2, an approximation to the interreflection component ($L^2_r(\theta_r,\theta_i,\phi_r-\phi_i;\theta_a)=L^2_{rp}(\theta_a)$) is given.

Once again, it is important to note that the radiance of the rough surface considered here is not constant with respect to the viewing direction $(\theta_r,\phi_r)$; it is non-Lambertian. We will study this behavior more closely in the following section.

## 4.3 Model for Gaussian Slope-Area Distribution

The surface considered above consists of V-cavities with equal facet slope. Realistic surfaces can be modeled only if the slope-area distribution $P(\theta_a,\phi_a)$ includes a variety of different facet slopes. If the surface roughness is isotropic, the slope-area distribution can be described using a single parameter namely $\theta_a$ since the facets are uniformly distributed in $\phi_a$. The radiance of any isotropic surface can therefore be determined as:

$$L_r(\theta_r,\theta_i,\phi_r-\phi_i)=\int_0^{\frac{\pi}{2}} P(\theta_a)L_{rp}(\theta_a)\,\sin\theta_a\,d\theta_a \tag{25}$$

where the source illumination (no interreflection) component of $L_{rp}(\theta_a)$ is given by (24). We assume the isotropic distribution to be Gaussian with mean $\mu$ and standard deviation $\sigma$, i.e. $P(\theta_a;\sigma,\mu)$.

[5] Imagine a V-cavity rotated about the global surface normal for any given source and sensor direction. Various masking/shadowing scenarios can be visualized.

Reasonably rough surfaces can be described using a zero mean ($\mu = 0$) Gaussian distribution:

$$P(\theta_a) \;=\; c\, e^{-\frac{\theta_a^2}{2\sigma^2}} \tag{26}$$

where the normalization constant $c$ is:

$$1/c = \int_{\theta_a=0}^{\frac{\pi}{2}} \int_{\phi_a=0}^{2\pi} e^{-\frac{\theta_a^2}{2\sigma^2}} \sin\theta_a \, d\phi_a \, d\theta_a$$

The reflectance model is to be obtained by substituting the radiance $L_{rp}^1(\theta_a)$ given by (24) and the Gaussian distribution $P(\theta_a; \sigma, 0)$ in integral (25). The resulting integral cannot be easily evaluated. Therefore, we pursued a functional approximation to the integral that is accurate for arbitrary surface roughness and angles of incidence and reflection. In deriving this approximation, we carefully studied the functional form of $L_{rp}^1(\theta_a)$ given by (24). This enabled us to identify basis functions that can be used in the approximation. Then, we conducted a large set of numerical evaluations of the integral in (25) by varying surface roughness $\sigma$, the angles of incidence $(\theta_i, \phi_i)$ and reflection $(\theta_r, \phi_r)$. These simulations and the identified basis functions were used to arrive at an accurate functional approximation for surface radiance. This procedure was applied independently to the direct illumination component as well as the interreflection component.

The final approximation results are given below. Once again, let $\alpha = Max[\theta_r, \theta_i]$ and $\beta = Min[\theta_r, \theta_i]$. The direct illumination component of radiance of a surface with roughness $\sigma$ is:

$$\begin{aligned} L_r^1(\theta_r, \theta_i, \phi_r - \phi_i; \sigma) = \tfrac{\rho}{\pi} E_0 \cos\theta_i \Bigg[ & C_1(\sigma) + \\ & \cos(\phi_r - \phi_i) C_2(\alpha; \beta; \phi_r - \phi_i; \sigma) \tan\beta + \\ & \Big(1 - |\cos(\phi_r - \phi_i)|\Big) C_3(\alpha; \beta; \sigma) \tan\left(\frac{\alpha + \beta}{2}\right) \Bigg] \end{aligned} \tag{27}$$

where the coefficients are:

$$C_1 = 1 - 0.5 \frac{\sigma^2}{\sigma^2 + 0.33}$$

$$C_2 = \begin{cases} 0.45 \frac{\sigma^2}{\sigma^2 + 0.09} \sin\alpha & \text{if } \cos(\phi_r - \phi_i) \geq 0 \\ 0.45 \frac{\sigma^2}{\sigma^2 + 0.09} \left( \sin\alpha - (\frac{2\beta}{\pi})^3 \right) & \text{otherwise} \end{cases}$$

$$C_3 = 0.125 \left( \frac{\sigma^2}{\sigma^2 + 0.09} \right) \left( \frac{4\alpha\beta}{\pi^2} \right)^2$$

Using a similar approach, an approximation to the interreflection component was also derived. In this case, the interreflection component for the single-slope isotropic surface (Appendix B.2) was used to guess the basis functions. The final approximation to the interreflection component of radiance for a surface with roughness $\sigma$ is:

$$\begin{aligned} & L_r^2(\theta_r, \theta_i, \phi_r - \phi_i; \sigma) = \\ & 0.17 \frac{\rho^2}{\pi} E_0 \cos\theta_i \, \frac{\sigma^2}{\sigma^2 + 0.13} \left[ 1 - \cos(\phi_r - \phi_i) \left( \frac{2\beta}{\pi} \right)^2 \right] \end{aligned} \tag{28}$$

The two components are combined to obtain the total surface radiance:

$$\begin{aligned} & L_r(\theta_r, \theta_i, \phi_r - \phi_i; \sigma) = \\ & L_r^1(\theta_r, \theta_i, \phi_r - \phi_i; \sigma) \; + \; L_r^2(\theta_r, \theta_i, \phi_r - \phi_i; \sigma) \end{aligned} \tag{29}$$

If the surface is extremely rough, causing the zero-mean Gaussian model to be an inaccurate approximation, an additional parameter can be used to weight the interreflection component. Our simulations show that this enables the model to stretch a bit beyond its theoretical limits. Finally, the *BRDF* of the surface is obtained from its radiance and irradiance as $f_r(\theta_r, \theta_i, \phi_r - \phi_i; \sigma) = L_r(\theta_r, \theta_i, \phi_r - \phi_i; \sigma) \,/\, E_0 \cos\theta_i$. It is important to note that the above model obeys Helmholtz's reciprocity principle (see [2]). *Also note that the model reduces to the Lambertian model*[6] *when* $\sigma = 0$. Note that by substituting the albedo as function of the wavelength, $\rho(\lambda)$, the dependency of the model on the wavelength comes out explicitly.

In the next section, we present several experimental results that verify the derived reflectance model. Here, we give a brief illustration of the main characteristics of the model. Figure 8 shows the reflectance predicted by the model for a very rough surface with $\sigma = 30°$ and $\rho = 0.9$. The radiance $L_r$ in the plane of incidence $(\phi_r = \phi_i, \phi_i + \pi)$ is plotted as a function of the reflection angle $\theta_r$ for incidence angle $\theta_i = 75°$. Two curves are shown in the figure, both obtained by numerical evaluation of the integral in (25). Shortly, we shall examine the accuracy of the functional approximation.

The first curve (solid line) includes both direct illumination and interreflection components of radiance, while the second (thin line) is only the direct illumination component. Notice that these

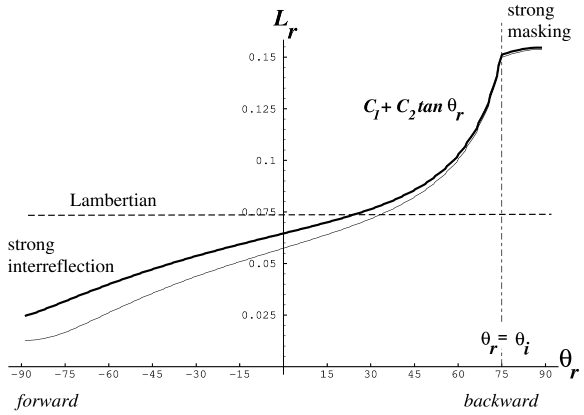


Figure 8: Diffuse reflectance in the plane of incidence for a surface with $\sigma = 30°$, $\rho = 0.90$, and incidence angle $\theta_i = 75°$. The thin line is radiance due to direct illumination (without interreflections).

radiance plots deviate substantially from Lambertian reflectance. *Surface radiance increases as the viewing direction approaches the source direction.* The curves can be divided into three sections. In the *backward* (source) direction, the radiance is maximum and gets "cut-off" due to strong masking effects when $\theta_r$ exceeds $\theta_i$. This cut-off occurs exactly at $\theta_r = \theta_i$ and is independent of roughness. In the middle section of the plot, radiance varies approximately as a scaled $tan\,\theta_r$ function with constant offset. Finally, interreflections dominate in the *forward* direction where most facets are self-shadowed and the visible facets receive light primarily from adjacent facets. This is illustrated by the difference between the two curves.

Figure 9 shows the effect of varying surface roughness. When $\sigma = 0$, the model predicts exactly Lambertian reflectance. The deviation from Lambertian behavior increases dramatically with roughness. In Figure 10, the effect of varying the incidence angle $\theta_i$ is shown. Here we have chosen to plot $BRDF$ rather than radiance to better illustrate the effect of varying $\theta_i$. It is interesting

[6] When $\sigma = 0$, $C_1 = 1$, $C_2 = 0$, and $C_3 = 0$, yielding $L_r^1 = \frac{\rho}{\pi} E_0 \cos\theta_i$.

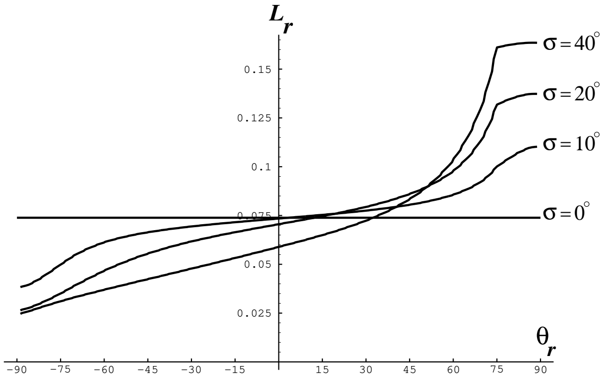


Figure 9: Effect of roughness $\sigma$ on surface radiance ($\theta_i = 75°$ and $\rho = 0.9$).

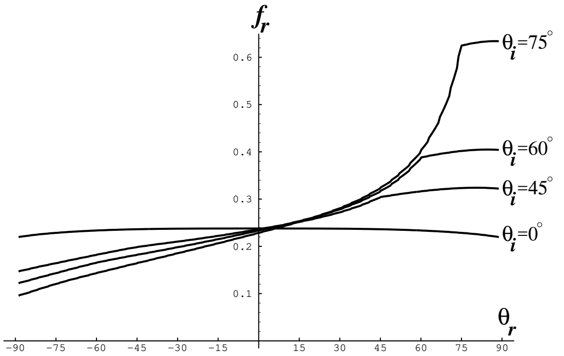


Figure 10: *BRDF* for different angles of incidence. $\sigma = 40°$ and $\rho = 0.9$.

to note that the model predicts near-Lambertian behavior for very small incidence angles ($\theta_i \approx 0$). This results from both facets of a V-cavity having nearly equal irradiance for small angles of incidence. As the incidence angle increases, the backscatter phenomenon begins to dominate. Figure 11 shows the effect of placing the sensor outside the plane of incidence. When the sensor-normal plane is perpendicular to the source-normal plane, the rough surface again exhibits near-Lambertian characteristics.

Figure 12 shows comparisons between radiance values computed by numerical evaluation of (25) (thick line) and the functional approximation (thin line) given by (27) and (28). Once again, radiance is measured in the plane of incidence ($\phi_r = \phi_i, \phi_i + \pi$). In all cases, the functional approximation proves to be very accurate.

## 4.4 Qualitative Model

In this section, we propose a further simplification to the reflectance model presented in the previous section. In order to obtain this simplification, a slight sacrifice in accuracy must be made. In return, some computations can be saved during image rendering. The following simplified model was arrived at by studying, through numerous simulations, the relative significance of various terms in the functional approximation given by (27). The simulations showed that coefficient $C_3$ makes a relatively small contribution to the total radiance. A simpler model is thus obtained by discarding $C_3$ and ignoring interreflections:

$$L_r(\theta_r, \theta_i, \phi_r - \phi_i; \sigma) = \tag{30}$$

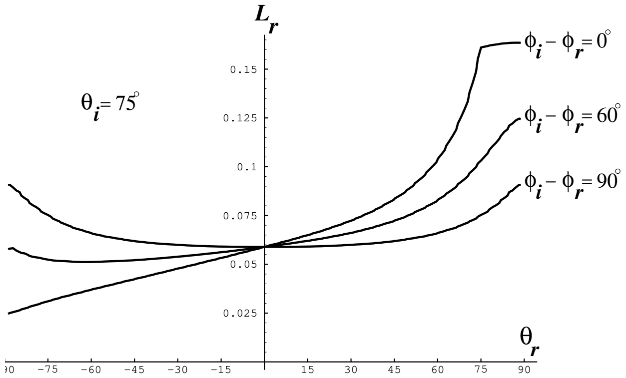


Figure 11: Radiance outside the plane of incidence. $\sigma = 40°$ and $\rho = 0.9$.

$$\frac{\rho}{\pi} E_0 \cos\theta_i (A + B\,Max\left[0, \cos(\phi_r - \phi_i)\right] \sin\alpha \tan\beta)$$

$$A = 1.0 - 0.5\frac{\sigma^2}{\sigma^2 + 0.33}$$

$$B = 0.45\frac{\sigma^2}{\sigma^2 + 0.09}$$

The two coeffcients $A$ and $B$ are obtained directly from $C_1$ and $C_2$, respectively. Note that the qualitative model also reduces to the Lambertian model when $\sigma = 0$. In Figure 13, we have compared the qualitative model with the numerical evaluation of the model[7]. This model can be of significant practical value in applications where high accuracy is not critical.

# 5 Experimental Verification

We have conducted several experiments to verify the accuracy of the reflectance model. The experimental set-up used to measure the radiance of samples is shown in Figure 14. In the case of outdoor scenes, each sensor element (pixel) typically includes a large surface area (several inches in dimensions and often more). Commercially available reflectance measurement devices are applicable only to small samples. Consequently, we developed our own measurement device. Each sample is approximately 2×2 inches. It is imaged using a 512×480 pixel CCD camera that is mounted at the end of a 6 foot long beam. The other end of the beam is attached to a rotary stage to facilitate precise variation of the viewing angle $\theta_r$. The sample is illuminated using a 300 Watt incandescent light source. The solid angles subtended by the sensor and source from the sample are approximately $d\omega_i = 0.003$ steradians and $d\omega_r = 0.0009$ steradians, respectively. The illumination direction $(\theta_i, \phi_i)$ is adjusted manually. Images of the sample are digitized and the radiance is computed as the average brightness over all pixels within an image window that lies on the sample. The image window size is varied as a function of sensor direction to ensure that the same area on the sample is always used.

Figure 15 shows results obtained for a sample of wall plaster. The sample has matte local reflectance properties but is very rough; it is exactly the type of surface that our reflectance model characterizes. Reflectance is represented by the normalized radiance $L_r(\theta_r)/L_r(0)$ where $L_r(0)$ is the radiance measured when the sample is viewed from the normal direction. The normalized

[7] Discrepancies caused by the lack of the interreflection component in the qualitative model can be partially compensated by replacing the constant $0.33$ in coefficient $A$ with $0.57$.

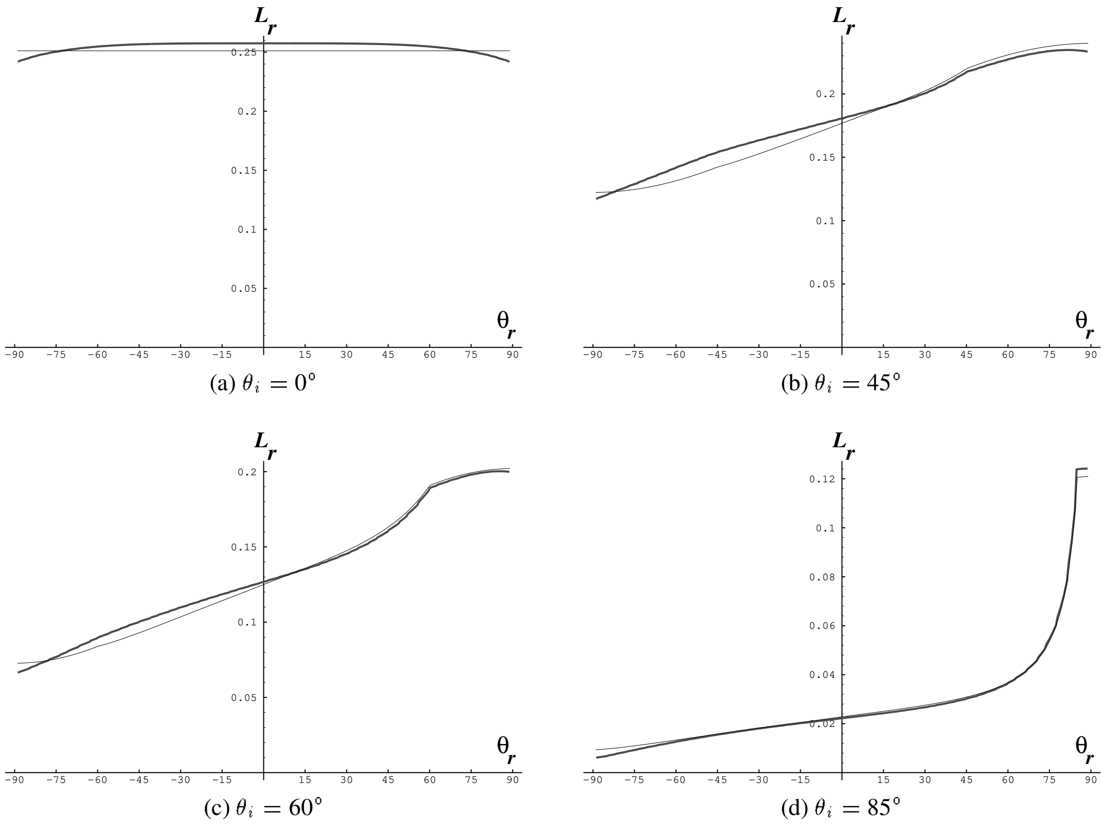


Figure 12: Comparison between numerical evaluation of the model (thick line) and functional approximation (thin line) for a surface with $\sigma = 30°$ and $\rho = 0.90$.

radiance is also equal to the normalized $BRDF\ f_r(\theta_r)/f_r(0)$. The radiance of each sample is plotted as a function of the sensor direction $\theta_r$ for different angles of incidence $\theta_i$. These measurements are made in the plane of incidence ($\phi_r = \phi_i = 0$). The dots represent measured radiance values while the solid lines are predictions obtained using the reflectance model for Gaussian surface roughness. In these initial experiments, $\sigma$ was empirically selected to obtain the best match between measured and predicted reflectance. Here, we have used the numerical evaluation of the model (equation 25). This was done to demonstrate not only the accuracy of the model but also the validity of all assumptions made while developing the model.

Similar results are presented in Figures 16 and 17 for sample B (painted sand paper) and sample C (white sand). For all three samples, radiance increases as the viewing direction $\theta_r$ approaches the source direction $\theta_i$ (backward reflection). This is in contrast to the behavior of rough specular surfaces that reflect more in the forward direction, or Lambertian surfaces where radiance does not vary with viewing direction. For all three samples, the model predictions and experimental measurements match remarkably well. In all cases, a small peak is noticed near the source direction. This phenomenon was discussed earlier in the paper and is different from the one described by our model; it is the backscatter peak studied by several researchers [13] [24] [12] [19] [32] and discussed in the context of graphics rendering by [28]. Some of the discrepancies between the model and measured data in the forward direction can be attributed to the long V-cavity assumption. In the case of sample C (sand), we see a small specular component in the forward direction. This is due to the specular characteristics of individual sand particles. In Figure 18, we have shown measurements obtained outside the plane of incidence ($\phi_r \neq 0$) for sample C. These measurements are a critical measure of the accuracy of any reflectance model but are seldom found in reflectance literature. Once again, the model and measured data are in strong agreement.

Figures 19 through 21 show results for samples that have not only a body reflectance component but also a significant surface reflection component. These samples are included to show that surfaces with a surface reflection component can also exhibit the backscattering phenomenon that the new model describes. In these experiments, the reflectance model used is a linear combination of new model and the Torrance-Sparrow model [31] that describes the incoherent directional component of surface of reflection. We selected this model as it is based on exactly the same surface roughness assumptions (symmetric, long, V-cavities) as the present model. The radiance predicted by the model is:

$$L_r^s \;=\; \frac{F(n)\mathcal{GAF}}{\cos\theta_r\,\cos\theta_a}\,e^{-\frac{\theta_a^2}{2\sigma^2}} \tag{31}$$

where, $F$ is the Fresnel reflection coefficient, and $n$ is the refractive index of the surface medium. The $\cos\theta_a$ in the denominator results from using the slope-area distribution instead of the facet-number distribution (see Section 3). This model predicts a peak in the forward direction (close to the specular direction) and the distribution of the reflected radiance gets wider with increase in surface roughness $\sigma$. The total radiance is expressed as a linear combination of the body and surface components:

$$L_r \;=\; k_b\,L_r^b \,+\, k_s\,L_r^s \tag{32}$$

where the body reflectance component $L_r^b$ is predicted by the model proposed in this paper. In these experiments, we used the functional

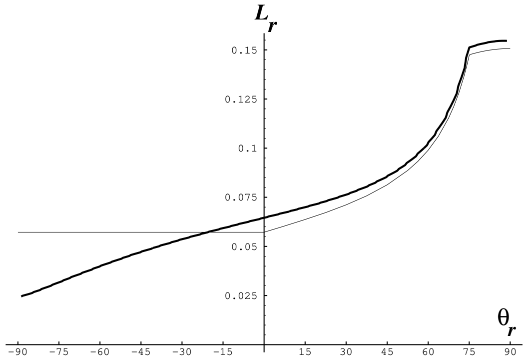

(a) $\phi_r - \phi_i = 0°$

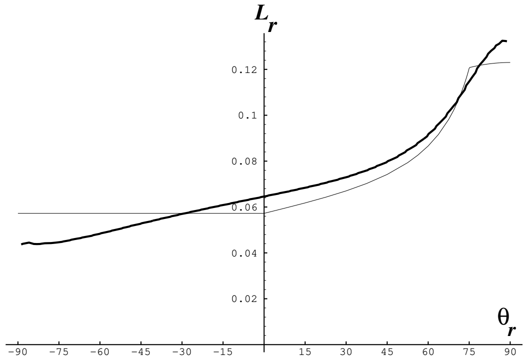

(b) $\phi_r - \phi_i = 45°$

Figure 13: Comparison between numerical evaluation (thick line) and the qualitative model (thin line): (a) in the plane of incidence ($\phi_r - \phi_i = 0°$), and (b) outside the plane of incidence. In both cases, $\sigma = 30°$, $\rho = 0.90$, and $\theta_i = 75°$.

approximation (27) instead of the numerical evaluation of integral (25). Moreover, the reflectance parameters $\sigma$, $\rho$, $k_b$, and $k_s$ were estimated by fitting (using non-linear optimization) the above model to measured data. Since it is difficult to obtain meaningful estimates of $n$ for the synthetic samples we have used, the effect of the Fresnel coefficient was ignored by assuming $F = 1$. Note that for all three samples, the proposed model does very well in describing the increase in radiance as the viewer approaches the source, as well as the cut-off in radiance that takes place in the source direction. This despite the fact that the three samples have roughness characteristics that differ from the V-cavity model. For the foam sample, the surface reflectance component (radiance increase in the forward direction) is described well by the Torrance-Sparrow model. The Torrance-Sparrow model does only reasonably well for the cloth towel and not very well for the wood-shaving sample. The main reason is the following: while the Gaussian roughness model appears explicitly in the Torrance-Sparrow model, it is integrated over all facet orientations in our case. As a result, our model is less sensitive to the actual surface roughness distribution than the Torrance-Sparrow model.

# 6 Implications for Graphics

In this section, we describe the implications of the proposed model for realistic rendering. Figure 22(a) shows a real image of the rough cylindrical clay vase discussed in the introduction. Figure 22(b) shows a rendered image of the vase using the Lambertian model and its known geometry. Clearly, this rendered image does not match the real image of the vase. On the other hand, the appearance of the rendered vase using the proposed reflectance

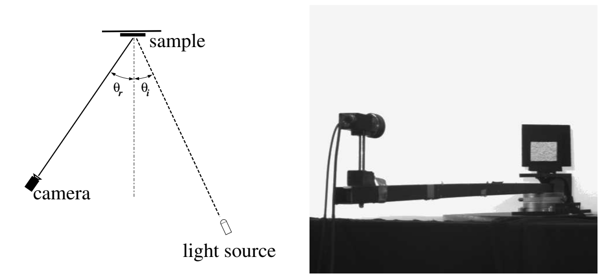

(a) (b)

Figure 14: (a) Sketch and (b) photograph of the set-up used to measure reflectance.

model, shown in Figure 22(c), closely resembles the real vase. The model parameters $\rho = 0.7$ and $\sigma = 40°$ were chosen empirically to obtain the best fit to the measured brightness values. Figure 23(a) compares brightness values along the cross-section of the three different vase images in Figure 22. It is interesting to note that the brightness of the real vase remains nearly constant over most of the cross-section and drops quickly to zero very close to the limbs. The proposed model does very well in predicting this behavior, while the Lambertian model produces large brightness errors. Figure 23(b) shows similar plots for illumination from 20° to the right of the sensor. In this case, brightness variation on the real vase is asymmetric. Once again, the proposed model closely matches the real image. However, the Lambertian model forces the brightness close to the right limb of the vase to drop much faster than in the real image. As a result, the brightness peak predicted by the Lambertian model is significantly away from the actual peak.

The functional approximation, given by equation (27), and the qualitative model, given by (30), are easily used for realistic rendering. We have implemented the functional approximation as a "shader" using the RenderMan shading language [33]. The rendered figures are provided as additional tiff files. The first image (in the file "spheres.tif") shows spheres rendered using the shader. In all four cases, the sphere is illuminated from the viewer direction. In the first case (the leftmost sphere), $\sigma = 0°$, and hence the sphere appears Lambertian. The roughness parameters of the other spheres to right are: $\sigma = 10°$, $\sigma = 20°$ and $\sigma = 40°$, in that order. As the roughness increases, the sphere begins to appear flatter. In the extreme roughness case, as in the rightmost sphere, the sphere appears like a flat disc with near constant brightness. This phenomenon has been widely observed and reported in the case of the full moon ([26],[29]).

Finally, the four images named "scene" (in the files named: "scene.1.tif",..., "scene.4.tif") show rendered images of a scene with three matte objects, a vase, cylindrical block and a cube. In the first image, (file "scene.1.tif"), all three objects have zero macroscopic roughness, i.e. they are Lambertian. Illumination in this case is from the viewer direction. Note that the vase and the cylinder have strong brightness variations, and the three visible faces of the cube have distinctly different brightness values. In the second image (file "scene.2.tif"), the scene is again illuminated from the viewer direction, but the three objects have roughness $\sigma = 30°$. Consequently, the shading over the vase and the cylinder is diminished considerably. Furthermore, the contrast between the flat and curved sections of the cylindrical block and also the contrast between the three faces of the cube are reduced substantially. It is important to note that the moderate shading is achieved without any ambient component in the illumination, but rather from modeling of roughness effects. In the third and the fourth images (files "scene.3.tif" and "scene.4.tif"), the three objects have the same

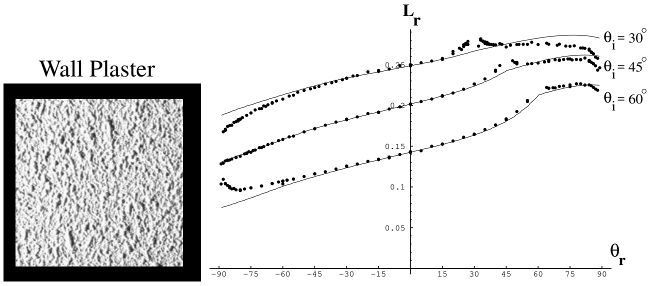


Figure 15: Reflectance measurement and reflectance model (using $\sigma = 30°$, $\rho = 0.90$) plots for wall plaster (sample A). Radiance is plotted as a function of sensor direction $(\theta_r)$ for different angles of incidence $(\theta_i = 30°, 45°, 60°)$.

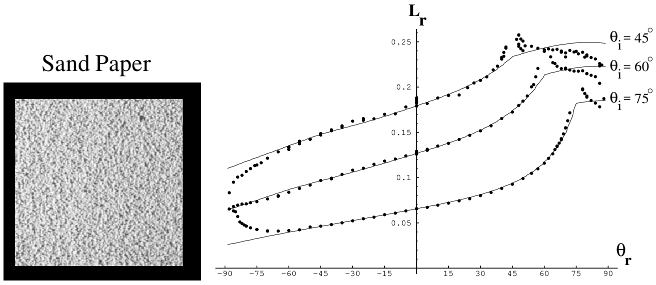


Figure 16: Reflectance measurement and reflectance model (using $\sigma = 40°$, $\rho = 0.80$) plots for painted sand-paper (sample B).

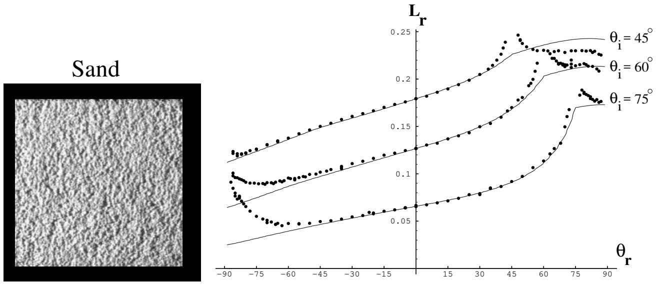


Figure 17: Reflectance measurement and reflectance model (using $\sigma = 35°$, $\rho = 0.80$) plots for white sand (sample C).

roughness values as in the first and second images respectively, but the scene is illuminated from 20 degrees to the right of the viewing direction. Again, shading differences are seen in the two images, though less than when the scene is illuminated from the viewing direction.

## 7 Summary

In conclusion, we have developed a comprehensive model for body reflectance from surfaces with macroscopic roughness. A model was first derived for anisotropic surfaces that have facets with only one slope. This result was used to develop a model for isotropic surfaces with Gaussian slope-area distribution. We have also presented a qualitative model for diffuse reflection that has a simple functional form. Numerous experiments were conducted to verify the reflectance mechanism described in this paper. Real and rendered images of diffuse objects were compared to demonstrate that the proposed model has important implications for computer graphics.

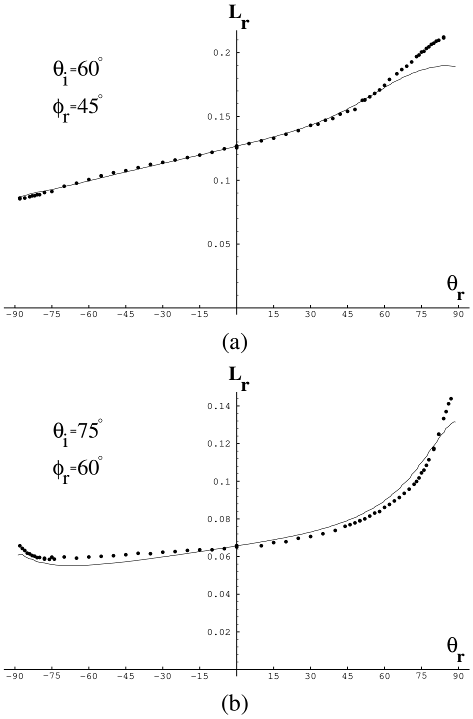


Figure 18: Reflectance measurement and reflectance model plots for sample C. These measurements were obtained for sensor directions outside the plane of incidence: (a) $\theta_i = 60°$ and $\phi_r = 45°$ ; and (b) $\theta_i = 75°$ and $\phi_r = 60°$.

# Appendix

## A Derivation of the Geometric Attenuation Factor

In this appendix we present the details of the derivation of the geometric attenuation factor for arbitrary source, viewer and facet normal directions.

### $\mathcal{GAF}$ for Perpendicular V-Cavities:

We first restrict ourselves to V-cavities that are oriented perpendicular to the sensor-source plane. Later, the analysis is extended to arbitrary sensor and source directions. Figure 6 illustrates the masking and shadowing phenomena for the case of perpendicular V-cavities. Our objective is to determine, for a given source direction $\hat{s}$ and sensor direction $\hat{v}$ the fraction of facet area that is illuminated and visible. If the visible area is smaller than the illuminated area, masking dominates. Likewise, if the illuminated area is smaller than the visible area, shadowing dominates. We denote the length (extent on the surface plane) and width of the facet by $l$ and $w$, respectively. Further, $m_s$ and $m_v$ are sections of the facet that are shadowed and masked, respectively. The area of a facet that is both illuminated and visible is $l \cdot Min[w - m_s, w - m_v]$. The $\mathcal{GAF}$ is obtained by dividing this expression by the area $w\, l$ of the facet:

$$\mathcal{GAF} \;=\; Min\left[1 - \frac{m_s}{w},\; 1 - \frac{m_v}{w}\right] \tag{33}$$

We would like to express the $\mathcal{GAF}$ in terms of the angles of incidence (source) and reflection (sensor). From the triangle $(w; m_s; n)$

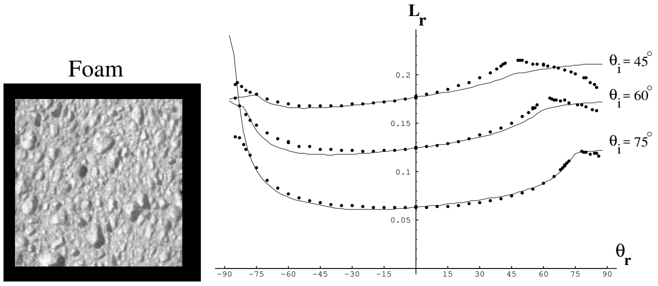


Figure 19: Reflectance measurement and reflectance model ($\sigma = 20°$, $\rho = 0.8$, $k_s/k_b = 0.019$) plots for foam (sample D).

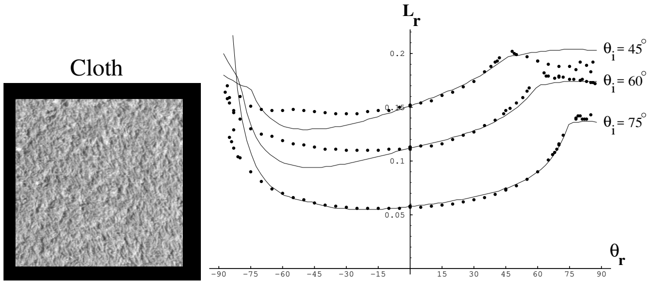


Figure 20: Reflectance measurement and reflectance model ($\sigma = 42°$, $\rho = 0.75$, $k_s/k_b = 0.085$) plots for a cotton towel (sample E).

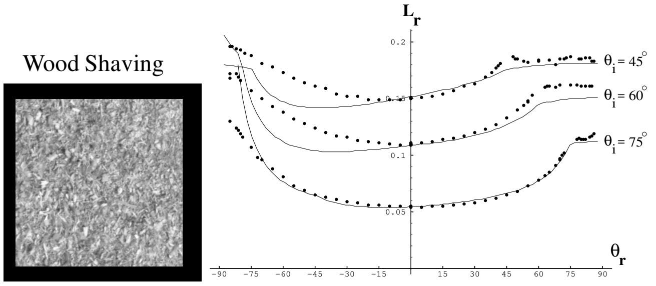


Figure 21: Reflectance measurement and reflectance model (using $\sigma = 26°$, $\rho = 0.7$, $k_s/k_b = 0.043$) plots for fine wood shavings (sample F).

in Figure 6, we have:

$$\begin{aligned} n \sin\theta_i &= m_s \cos\theta_a + w \cos\theta_a \\ n \cos\theta_i &= -m_s \sin\theta_a + w \sin\theta_a \end{aligned} \tag{34}$$

By multiplying the first expression by $\cos\theta_i$ and the second by $-\sin\theta_i$ and adding the results we get:

$$\frac{m_s}{w} = -\frac{\cos(\theta_a + \theta_i)}{\cos(\theta_a - \theta_i)} \tag{35}$$

or

$$1 - \frac{m_s}{w} = \frac{2\cos\theta_a \cos\theta_i}{\cos(\theta_a - \theta_i)}$$

In the above expression, the angles $\theta_i$ and $\theta_r$ are positive in the counter-clockwise direction and negative in the clockwise direction. It can be easily shown that there is no shadowing when $|\ \theta_a + \theta_i\ | \leq \frac{\pi}{2}$ and $|\ \theta_a - \theta_i\ | \leq \frac{\pi}{2}$, i.e. $1 - \frac{m_s}{w} \geq 1$. On the other hand, the entire facet is shadowed if $|\ \theta_i - \theta_a\ | \geq \frac{\pi}{2}$, i.e. $1 - \frac{m_s}{w} \leq 0$. A similar result is obtained for masking. All these conditions are included in the following $\mathcal{GAF}$ expression for perpendicular V-cavities:

$$\mathcal{GAF} = Min\left[1, Max\left[0, \frac{2\cos\theta_i \cos\theta_a}{\cos(\theta_i - \theta_a)}, \frac{2\cos\theta_r \cos\theta_a}{\cos(\theta_r - \theta_a)}\right]\right] \tag{36}$$

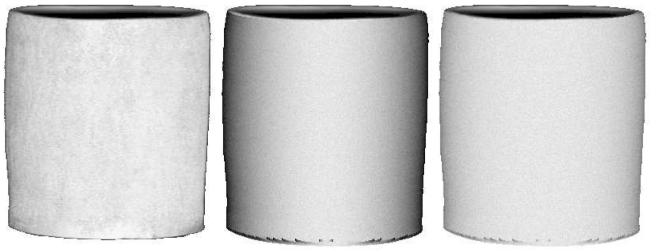

(a) Image (b) Lambertian (c) Model

Figure 22: Real image of a cylindrical clay vase compared with images rendered using the Lambertian and proposed models. Illumination is from the camera direction.

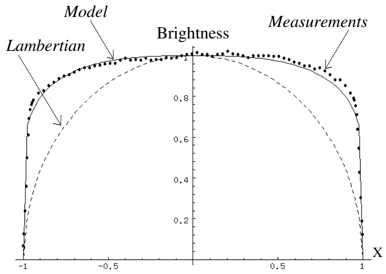


(a) $\theta_i = 0°$

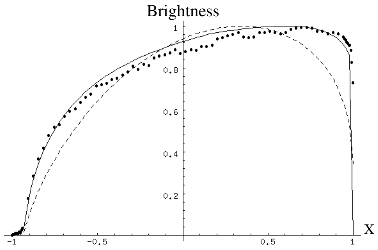


(b) $\theta_i = 20°$

Figure 23: Comparison between image brightness along the cross-section of the real vase, and vases rendered using the Lambertian and proposed models.

**$\mathcal{GAF}$ for the General Case:**

In the general case, source and sensor directions are arbitrary and can lie outside the plane perpendicular to the V-cavity. To make the masking/shadowing calculations tractable, we invoke the assumption that the length of facets is large compared to their width[8], i.e. $l \gg w$. Then, the analysis of masking and shadowing is reduced to the perpendicular V-cavity case by projecting the source direction $\hat{s}$ and sensor direction $\hat{v}$ onto the plane perpendicular to the cavity. These projections are done using basic trigonometry as shown in Figure 24. The projected angles are then substituted into (36), in place of $\theta_i$ and $\theta_r$, to obtain the general $\mathcal{GAF}$ expression:

$$\mathcal{GAF} = Min\left[1, Max\left[0, \frac{2\cos\theta_i \cos\theta_a}{\cos\theta_i \cos\theta_a + \sin\theta_i \sin\theta_a \cos(\phi_i - \phi_a)}, \right.\right. \tag{37}$$

[8] When facet length is much larger than facet width, the exact shape of the cast shadow at the two ends of the facet can be ignored.

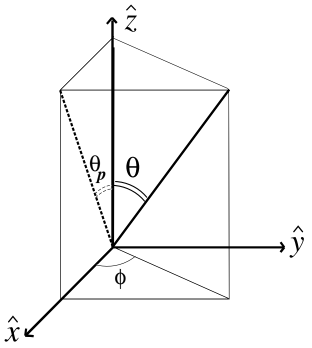


$$
\begin{aligned}
\sin\theta_p &= \frac{\sin\theta\cos\phi}{\sqrt{\cos^2\theta + \sin^2\theta\cos^2\phi}} \\
\cos\theta_p &= \frac{\cos\theta}{\sqrt{\cos^2\theta + \sin^2\theta\cos^2\phi}} \\
\tan\theta_p &= \tan\theta\cos\phi
\end{aligned}
$$

Figure 24: Relationship between projected and actual angles.

$$\left.\left.\frac{2\cos\theta_r\cos\theta_a}{\cos\theta_r\cos\theta_a + \sin\theta_r\sin\theta_a\cos(\phi_r - \phi_a)}\right]\right]$$

Alternatively, the $\mathcal{GAF}$ can be expressed in terms of the source, sensor, facet normal, and surface normal vectors:

$$\mathcal{GAF} = Min\left[1, Max\left[0, \frac{2<\hat{s},\hat{n}><\hat{a},\hat{n}>}{<\hat{s},\hat{a}>}, \frac{2<\hat{v},\hat{n}><\hat{a},\hat{n}>}{<\hat{v},\hat{a}>}\right]\right] \quad (38)$$

# B Radiance of Isotropic Surface with Single-Slope Distribution

In this appendix, we outline derivations for the direct illumination and interreflection components of projected radiance for the isotropic surface discussed in Section 4.2. These results are used in Section 4.3 to derive the reflectance model for a surface with Gaussian slope-area distribution.

## B.1 Radiance due to Direct Illumination

Our objective here is to evaluate the integral in (23). For any given source direction $(\theta_i, \phi_i)$ and sensor direction $(\theta_r, \phi_r)$, facets on the isotropic surface could be masked, shadowed, masked and shadowed, or neither masked nor shadowed. The radiance for each of these cases is given in Table 1. The problem therefore is to decompose the integral in (23) into parts, each corresponding to a different masking/shadowing range. Using basic geometry, we have identified the limits of the integrals corresponding to different ranges of shadowing/masking. These limits are represented by the *critical angles* $\phi_c^i$ (for shadowing) and $\phi_c^r$ (for masking). The critical angle $\phi_c^i$ is related to the slope $\theta_a$ of surface facets:

$$\phi_c^i = \begin{cases} \cos^{-1}\left(\frac{1}{\tan\theta_a\tan\theta_i}\right) & \text{if } (\tan\theta_a\tan\theta_i) > 1 \\ 0 & \text{otherwise} \end{cases} \quad (39)$$

The angle $\phi_c^r$ is determined using the same expression by replacing $\theta_i$ with $\theta_r$. These critical angles are related to the masking/shadowing ranges as shown in Table 2.

Using the above critical angle expressions, Table 2, and Table 1, we decompose (23) into the sum of several integrals. Each integral can be evaluated for any fixed viewer direction. However, for arbitrary directions several cases arise and the results are not easy to use in practice. Therefore, we have chosen to express the radiance of the surface for any arbitrary viewing direction $(\theta_r, \phi_r)$ as a weighted sum of the radiance $L^1_{rp_{\parallel}}$ in the plane of incidence ($\phi_r = \phi_i, \phi_i + \pi$), and the radiance $L^1_{rp_{\perp}}$ in the perpendicular plane ($\phi_r = \phi_i \pm \frac{\pi}{2}$).

**Radiance in the Plane of Incidence:**

There are two cases to consider. In the first, $\phi_r = \phi_i$. Without loss of generality, we can assume $\phi_r = \phi_i = 0$. When $\theta_i \geq \theta_r$, radiance is obtained as:

$$
\begin{aligned}
L^1_{rp_{\parallel}}(\theta_a) = \tfrac{\rho}{\pi} E_0 \cos\theta_i \cos\theta_a \frac{1}{2\pi} \Bigg[ & \int_{-\phi_c^i}^{\phi_c^i} 2(1 + \tan\theta_a\tan\theta_r\cos\phi_a)\,d\phi_a + \\
& 2\int_{\phi_c^i}^{\pi-\phi_c^i} (1 + \tan\theta_a\tan\theta_i\cos\phi_a) (1 + \tan\theta_a\tan\theta_r\cos\phi_a)\,d\phi_a \Bigg] \\
= \tfrac{\rho}{\pi} E_0 \cos\theta_i\cos\theta_a \Bigg[ & 1 + 2\tan\theta_a\tan\theta_r \frac{\sin\phi_c^i}{\pi} + \frac{1}{2}\tan^2\theta_a\tan\theta_i\tan\theta_r \left(1 - \frac{2\phi_c^i + \sin(2\phi_c^i)}{\pi}\right)\Bigg]
\end{aligned}
\quad (40)
$$

When $\theta_r \geq \theta_i$, the sensor and source directions are simply switched in the expression inside the square brackets.

In the second case, $\phi_r = \phi_i + \pi$. Again, without loss of generality, we can assume $\phi_i = 0$, $\phi_r = \pi$. When $\theta_i \geq \theta_r$, we get:

$$
\begin{aligned}
L^1_{rp_{\parallel}}(\theta_a) = \tfrac{\rho}{\pi} E_0 \cos\theta_i \cos\theta_a \frac{1}{2\pi} \Bigg[ & 2\int_{\phi_c^r}^{\phi_c^i} 2(1 + \tan\theta_a\tan\theta_r\cos(\pi - \phi_a))\,d\phi_a + \\
& 2\int_{\phi_c^i}^{\pi-\phi_c^i} (1 + \tan\theta_a\tan\theta_i\cos\phi_a) (1 + \tan\theta_a\tan\theta_r\cos(\pi-\phi_a))\,d\phi_a \Bigg] = \\
\tfrac{\rho}{\pi} E_0 \cos\theta_i\cos\theta_a \Bigg[ & 1 - \frac{2\phi_c^r}{\pi} + 2\tan\theta_a\tan\theta_r \frac{\sin\phi_c^r - \sin\phi_c^i}{\pi} - \frac{1}{2}\tan^2\theta_a\tan\theta_i\tan\theta_r \left(1 - \frac{2\phi_c^i + \sin(2\phi_c^i)}{\pi}\right)\Bigg]
\end{aligned}
\quad (41)
$$

| Partial Shadow | No Shadow | Complete Self-Shadow |
|---|---|---|
| $\lvert\phi_a-\phi_i\rvert<\phi_c^i$ | $\phi_c^i\le\lvert\phi_a-\phi_i\rvert\le\pi-\phi_c^i$ | $\lvert\phi_a-(\phi_i+\pi)\rvert<\phi_c^i$ |
| Partial Masking | No Masking | Complete Self-Masking |
| $\lvert\phi_a-\phi_r\rvert<\phi_c^r$ | $\phi_c^r\le\lvert\phi_a-\phi_r\rvert\le\pi-\phi_c^r$ | $\lvert\phi_a-(\phi_r+\pi)\rvert<\phi_c^r$ |

Table 2: Masking/shadowing and the critical angles.

Once again, when $\theta_r \geq \theta_i$, the sensor and source directions are switched in the term inside the square brackets.

**Radiance in the Perpendicular Plane:**

We now calculate radiance for the case where the viewer is in the plane perpendicular to the plane of incidence; i.e. $\phi_r = \phi_i \pm \frac{\pi}{2}$. Again, there are two cases to be considered. In the first case, $\phi_c^i + \phi_c^r \leq \frac{\pi}{2}$. Here, the regions of shadowing and masking do not overlap. Using these limits, the integral in (23) is evaluated as:

$$L^1_{rp_\perp}(\theta_a) = \tfrac{\rho}{\pi} E_0 \cos\theta_i \cos\theta_a \tag{42}$$

In the second case, we have $\phi_c^i + \phi_c^r > \frac{\pi}{2}$. Here, the regions of masking and shadowing do overlap. Without loss of generality, we can choose $\phi_i = 0$ and $\phi_r = \frac{\pi}{2}$. We define the angle $\gamma$, $0 \leq \gamma \leq \frac{\pi}{2}$, that separates the regions of shadowing ($-\frac{\pi}{2} + \phi_c^r \leq \phi_a \leq \gamma$) and masking ($\gamma \leq \phi_a \leq \pi - \phi_c^i$). $\gamma$ is determined as: $\tan\theta_i \cos\gamma = \tan\theta_r \cos(\frac{\pi}{2} - \gamma)$. Then, the expression for radiance is:

$$\begin{aligned} L^1_{rp_\perp}(\theta_a) &= \tfrac{\rho}{\pi} E_0 \cos\theta_i \cos\theta_a \frac{1}{2\pi}\Bigg[ \int_{-\frac{\pi}{2}+\phi_c^r}^{\gamma} 2(1+\tan\theta_r\tan\theta_a\cos(\phi_a-\tfrac{\pi}{2}))d\phi_a + \\ &\qquad \int_{\gamma}^{\pi-\phi_c^i} 2(1+\tan\theta_i\tan\theta_a\cos\phi_a)d\phi_a\Bigg] = \\ &\tfrac{\rho}{\pi} E_0 \cos\theta_i\cos\theta_a\Bigg[1+\frac{1}{2}-\frac{\phi_c^i+\phi_c^r}{\pi} + \\ &\frac{\sqrt{\tan^2\theta_r\tan^2\theta_a-1}}{\pi} + \frac{\sqrt{\tan^2\theta_i\tan^2\theta_a-1}}{\pi} - \\ &\qquad \frac{\tan\theta_a\sqrt{\tan^2\theta_i+\tan^2\theta_r}}{\pi}\Bigg] \end{aligned} \tag{43}$$

**Radiance in Arbitrary Azimuth Angles:**

We have determined via simulations that the radiance of the isotropic surface in any arbitrary direction is well-approximated by the following weighted sum of $L^1_{rp_\parallel}(\theta_a)$ and $L^1_{rp_\perp}(\theta_a)$:

$$\begin{aligned} L_{rp}(\theta_a) \approx &\mid\cos(\phi_r-\phi_i)\mid L_{rp_\parallel}(\theta_a) + \\ &(1-\mid\cos(\phi_r-\phi_i)\mid)L_{rp_\perp}(\theta_a) \end{aligned} \tag{44}$$

This approximation was obtained by studying the expressions for the radiance components in the two planes. It is in general very accurate, with a slight over-estimation only for $\theta_r \approx \theta_i$ and $\theta_i \to \pi/2$.

Using the above linear combination of radiance in the two planes, we obtain the final expression for projected radiance. The following notation is used: $\alpha = Max[\theta_i, \theta_r]$ and $\beta = Min[\theta_i, \theta_r]$; if $\alpha = \theta_i$, $\phi_c^\alpha = \phi_c^i$, else $\phi_c^\alpha = \phi_c^r$; and the same rules apply to $\phi_c^\beta$.

$$\begin{aligned} L^1_{rp}(\theta_a) = \tfrac{\rho}{\pi} E_0\cos\theta_i\cos\theta_a\Bigg[1 + &\cos(\phi_r-\phi_i)\Big(A_1(\alpha;\theta_a)\tan\beta + A_2(\beta,\phi_r-\phi_i;\theta_a)\Big) + \\ &(1-\lvert\cos(\phi_r-\phi_i)\rvert)A_3(\theta_r,\theta_i;\theta_a)\Bigg] \end{aligned} \tag{45}$$

where the coefficients are:

$$A_1(\alpha;\theta_a) = \tan\theta_a\frac{2\sin\phi_c^\alpha}{\pi} + \frac{1}{2}\tan^2\theta_a\tan\alpha\left(1-\frac{2\phi_c^\alpha+\sin(2\phi_c^\alpha)}{\pi}\right)$$

$$A_2(\beta,\phi_r-\phi_i;\theta_a) = \begin{cases} \frac{2\phi_c^\beta}{\pi} - \tan\theta_a\,\tan\beta\,\frac{2\sin\phi_c^\beta}{\pi} & \text{if } \cos(\phi_r-\phi_i)<0 \\ 0 & \text{if } \cos(\phi_r-\phi_i)\geq 0 \end{cases}$$

$$A_3(\theta_r,\theta_i;\theta_a) = \begin{cases} 0 & \text{if } \phi_c^i+\phi_c^r\leq\frac{\pi}{2} \\ \frac{1}{2}-\frac{\phi_c^i+\phi_c^r}{\pi} + \frac{\sqrt{\tan^2\theta_r\tan^2\theta_a-1}}{\pi} + \frac{\sqrt{\tan^2\theta_i\tan^2\theta_a-1}}{\pi} - \frac{\tan\theta_a\sqrt{\tan^2\theta_i+\tan^2\theta_r}}{\pi} & \text{if } \phi_c^i+\phi_c^r>\frac{\pi}{2} \end{cases}$$

## B.2 Radiance due to Interreflections:

To calculate the radiance component due to interreflections, we need to evaluate the following integral:

$$L^2_{rp}(\theta_a) = \frac{1}{2\pi}\int_{\phi_a=0}^{2\pi} L^2_{rp}(\theta_a,\phi_a)d\phi_a \tag{46}$$

In Section 4.1.2, we found the interreflection factor ($\mathcal{IF}$) to be :

$$\mathcal{IF} = \tfrac{\pi}{2}\left[d(1,\frac{m_v}{w}) + d(1,\frac{m^s}{w}) - d(\frac{m^s}{w},\frac{m_v}{w}) - d(1,1)\right] \tag{47}$$

The above factor cannot be easily integrated. Therefore, we use the following approximation:

$$\mathcal{IF} \approx \pi(1-\cos\theta_a)(1-m^s)(1-m_v) \tag{48}$$

As in Appendix B.1, the regions of shadowing and masking were identified and the above approximation to $\mathcal{IF}$ was used to evaluate (46). The final expression for projected radiance of the isotropic surface due to interreflections is:

$$\begin{aligned} L^2_{rp}(\theta_a) \approx \frac{\rho^2}{\pi}E_0\cos\theta_i\cos\theta_a(1-\cos\theta_a)\Bigg[1 - &\cos(\phi_r-\phi_i)\Bigg(\frac{2\phi_c^\beta}{\pi} + 2\tan\theta_a\tan\beta\frac{\sin\phi_c^\alpha-\sin\phi_c^\beta}{\pi} + \\ &\frac{1}{2}\tan^2\theta_a\tan\alpha\tan\beta\left(1-\frac{2\phi_c^\alpha+\sin(2\phi_c^\alpha)}{\pi}\right)\Bigg)\Bigg] \end{aligned} \tag{49}$$

## REFERENCES


[1] P. Beckmann. Shadowing of random rough surfaces. *IEEE Transactions on Antennas and Propagation*, AP-13:384–388, 1965.

[2] P. Beckmann and A. Spizzichino. *The Scattering of Electromagnetic Waves from Rough Surfaces*. Pergamon, New York, 1963.

[3] J. F. Blinn. Models of light reflection for computer synthesized pictures. *ACM Computer Graphics (SIGGRAPH 77)*, 19(10):542–547, 1977.

[4] D. Buhl, W. J. Welch, and D. G. Rea. Reradiation and thermal emission from illuminated craters on the lunar surface. *Journal of Geophysical Research*, 73(16):5281–5295, August 1968.

[5] B. Cabral, N. Max, and R. Springmeyer. Bidirectional reflection functions from surface bump maps. *ACM Computer Graphics (SIGGRAPH 87)*, 21(4):273–281, 1987.

[6] S. Chandrasekhar. *Radiative Transfer*. Dover Publications, 1960.

[7] M. F. Cohen and D. P. Greenberg. The hemi-cube, a radiosity solution for complex environments. *ACM Computer Graphics (SIGGRAPH 85)*, 19(3):31–40, 1985.

[8] R. L. Cook and K. E. Torrance. A reflection model for computer graphics. *ACM Transactions on Graphics*, 1(1):7–24, 1982.

[9] D. Forsyth and A. Zisserman. Mutual illumination. *Proc. Conf. Computer Vision and Pattern Recognition*, pages 466–473, 1989.

[10] R. Hall. *Illumination and Color in Computer Generated Imagery*. Springer-Verlag, 1989.

[11] P. Hanrahan and W. Krueger. Reflection from layered surfaces due to subsurface scattering. *Computer Graphics Proceedings (SIGGRAPH 93)*, pages 165–174, 1993.

[12] B. W. Hapke, R. M. Nelson, and W. D. Smythe. The opposition effect of the moon: The contribution of coherent backscatter. *Science*, 260(23):509–511, April 1993.

[13] B. W. Hapke and Huge van Horn. Photometric studies of complex surfaces, with applications to the moon. *Journal of Geophysical Research*, 68(15):4545–4570, August 1963.

[14] X. D. He, K. E. Torrance, F. X. Sillion, and D. P. Greenberg. A comprehensive physical model for light reflection. *ACM Computer Graphics (SIGGRAPH 91)*, 25(4):175–186, 1991.

[15] R. G. Hering and T. F. Smith. Apparent radiation properties of a rough surface. *AIAA Progress in Astronautics and Aeronautics*, 23:337–361, 1970.

[16] M. Jakob. *Heat Transfer*. Wiley, 1957.

[17] J. T. Kajiya. Anisotropic reflection model. *ACM Computer Graphics (SIGGRAPH 91)*, 25(4):175–186, 1991.

[18] J. J. Koenderink and A. J. van Doorn. Geometrical modes as a general method to treat diffuse interreflections in radiometry. *Journal of the Optical Society of America*, 73(6):843–850, 1983.

[19] Y. Kuga and A. Ishimaru. Retroreflectance from a dense distribution of spherical particles. *Journal of the Optical Society of America A*, 1(8):831–835, August 1984.

[20] J. H. Lambert. Photometria sive de mensure de gratibus luminis, colorum umbrae. *Eberhard Klett*, 1760.

[21] M. Minnaert. The reciprocity principle in lunar photometry. *Astrophysical Journal*, 93:403–410, 1941.

[22] S. K. Nayar, K. Ikeuchi, and T. Kanade. Shape from interreflections. *International Journal of Computer Vision*, 6:3:173–195, 1991.

[23] F. E. Nicodemus, J. C. Richmond, and J. J. Hsia. *Geometrical Considerations and Nomenclature for Reflectance*. National Bureau of Standards, October 1977. Monograph No. 160.

[24] P. Oetking. Photometric studies of diffusely reflecting surfaces with application to the brightness of the moon. *Journal of Geophysical Research*, 71(10):2505–2513, May 1966.

[25] E. Opik. Photometric measures of the moon and the moon the earth-shine. *Publications de L'Observatorie Astronomical de L'Universite de Tartu*, 26(1):1–68, 1924.

[26] N. S. Orlova. Photometric relief of the lunar surface. *Astron. Z*, 33(1):93–100, 1956.

[27] P. Poulin and A. Fournier. A model for anisotropic reflection. *ACM Computer Graphics (SIGGRAPH 90)*, 24(4):273–282, 1990.

[28] T. Shibata, W. Frei, and M. Sutton. Digital correction of solar illumination and viewing angle artifacts in remotely sensed images. *Machine Processing of Remotely Sensed Data Symposium*, pages 169–177, 1981.

[29] R. Siegel and J. R. Howell. *Thermal Radiation Heat Transfer*. Hemisphere Publishing Corporation, third edition, 1972.

[30] B. G. Smith. Lunar surface roughness: Shadowing and thermal emission. *Journal of Geophysical Research*, 72(16):4059–4067, August 1967.

[31] K. Torrance and E. Sparrow. Theory for off-specular reflection from rough surfaces. *Journal of the Optical Society of America*, 57:1105–1114, September 1967.

[32] L. Tsang and A. Ishimaru. Backscattering enhancement of random discrete scatterers. *Journal of the Optical Society of America A*, 1(8):836–839, August 1984.

[33] S. Upstill. *The RenderMan Companion*. Addison Wesley, 1989.

[34] R. J. Wagner. Shadowing of randomly rough surfaces. *Journal of the Acoustical Society of America*, 41(1):138–147, June 1966.

[35] H.W. Westin, J.R. Arvo, and K.E. Torrance. Predicting reflectance functions from complex surfaces. *ACM Computer Graphics (SIGGRAPH 92)*, 26(2):255–264, 1992.

[36] T. Whitted. An improved illumination model for shaded display. *Communications of the ACM*, 23(6):343–349, 1980.